JOURNAL OF GEOPHYSICAL RESEARCH, VOL. 106, NO. B1, PAGES 771-785, JANUARY 10, 2001

Source parameters for the 1952 Kern County earthquake, California: A joint inversion of leveling and triangulation observations

Gerald W. Bawden
U.S. Geological Survey, Menlo Park, California

Abstract. Coseismic leveling and triangulation observations are used to determine the faulting geometry and slip distribution of the July 21, 1952, M_w 7.3 Kern County earthquake on the White Wolf fault. A singular value decomposition inversion is used to assess the ability of the geodetic network to resolve slip along a multisegment fault and shows that the network is sufficient to resolve slip along the surface rupture to a depth of 10 km. Below 10 km, the network can only resolve dip slip near the fault ends. The preferred source model is a two-segment right-stepping fault with a strike of 51° and a dip of 75° SW. The epicentral patch has deep (6-27 km) left-lateral oblique slip, while the northeastern patch has shallow (1-12.5 km) reverse slip. There is nearly uniform reverse slip (epicentral, 1.6 m; northeast, 1.9 m), with 3.6 m of left-lateral strike slip limited to the epicentral patch. The seismic moment is $M_o = 9.2 \pm 0.5 \times 10^{19}$ N m ($M_w = 7.2$). The signal-to-noise ratio of the leveling and triangulation data is reduced by 96% and 49%, respectively. The slip distribution from the preferred model matches regional geomorphic features and may provide a driving mechanism for regional shortening across the Comanche thrust and structural continuity with the Scodie seismic lineament to the northeast.

1. Introduction

The Kern County earthquake was one of the largest earthquakes in California during the twentieth century (M_L 7.7, M_w 7.3 [*Richter*, 1955; *Ben-Menahem*, 1978]), second only to the great 1906 San Francisco earthquake. The 1952 event ruptured 60 km of the White Wolf fault, north of the junction of the San Andreas and Garlock faults, and near a restraining bend in the San Andreas fault (Figure 1). Even though this earthquake was one of the most well-studied events in southern California at the time [*Oakeshott*, 1955], nearly 30 years elapsed until the first rigorous geodetic source models were published [*Dunbar et al.*, 1980; *Stein and Thatcher*, 1981]. Unfortunately, differences in the geometry and slip distribution between these models provide conflicting interpretations on the relationship between the White Wolf fault and a number of other active faults and structures throughout the region.

I present a simple source model for the Kern County earthquake based on a comprehensive analysis of the coseismic triangulation and leveling observations. This study differs from previous coseismic analysis by including a larger set of triangulation observations and by directly inverting the geodetic observations rather than using forward modeling techniques to match shear strain estimates and uplift patterns. Furthermore, I examine where the geodetic observations can resolve slip and, more importantly, where the resolution is poor and slip cannot be determined. I first constrain the geometry of the fault model by combining the geodetic data with aftershock locations and then invert the observations, in a least squares sense, to estimate the slip distribution along the White Wolf fault. Finally, I compare the results with previous studies and discuss the implications in a regional context.

Paper number 2000JB900315.

2. Geodetic Data

2.1. Triangulation

This study uses coseismic angle changes for the triangulation array that spans the White Wolf fault (Figure 2 and Table 1a). The U.S. Coast and Geodetic Survey (USCGS) collected over four decades (1926-1972) of triangulation data throughout the Big Bend region of the San Andreas fault [*Thatcher*, 1979; *Dunbar et al.*, 1980; *Stein and Thatcher*, 1981; *King and Savage*, 1984; *Eberhart-Phillips et al.*, 1990; *Snay et al.*, 1996; *Bawden et al.*, 1997], including two surveys that bracket the July 21, 1952 mainshock. Two months prior to the earthquake the USCGS completed a comprehensive, 6-month-long survey of the triangulation array that spans the southern half of the White Wolf fault; this array was again reoccupied beginning 2 months (September 1952 to January 1953) after the mainshock. Both the preseismic and postseismic surveys were conducted to first-order tolerances, where the standard error, σ, assigned to each measurement was based on the consistency of the angles turned during each setup and the consistency among different setups at the same station. The standard error values used in this study are $\leq$0.8 arc sec.

The 143 coseismic angle changes were calculated by differencing 654 preseismic and postseismic angles (Table 1b and Figure 2). If repeated measurements were made in either epoch (1951-1952 or 1952-1953), then the angle was determined by averaging each observation, weighted by its standard error. To assess the quality of the data, I evaluated the misclosures for monument combinations that formed a closed triangle, a total of 16 closed triangle (48 angles) for both preseismic and postseismi-

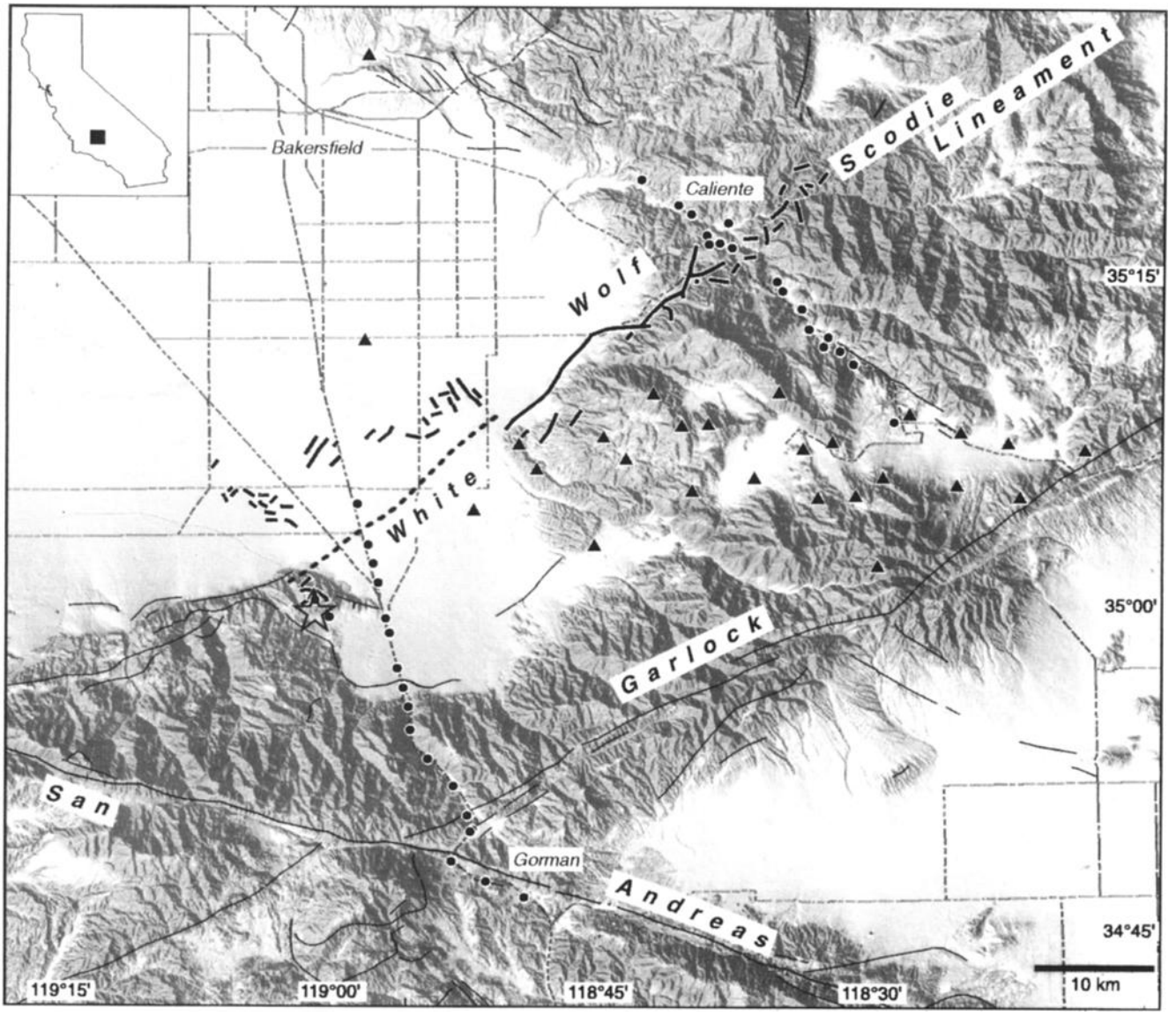

Figure 1. Topography, monument, and fault map of the White Wolf fault area. The 1952 surface ruptures are shown in bold black lines, dashed where buried. Star, 1952 epicenter; triangles, triangulation stations; circles, leveling benchmarks. . The figure generated with GMT [*Wessel and Smith*, 1991].

c epochs. If the misclosure was larger than the sum of the errors in the three angle measurements, then the misclosure was distributed equally among the three measurements [*Bomford*, 1980; *Hodgkinson et al.*, 1996]. Such misclosure adjustments were made to 12 of the 654 observations.

The signal available for modeling is best described by the signal-to-noise ratio (S/N). The signal represented here is the coseismic angle change, and the standard deviation of each angle change is set to 1.18 arc sec. The standard deviation is based on the weighted average of the triangle closures [*King and Thatcher*, 1998] and is consistent with first-order uncertainties ($0.8\sqrt{2}$) typically assigned to triangulation observations [*Gergen*, 1975]. The signal-to-noise ratio can be expressed as

$$\mathrm{S/N} = \left[\frac{1}{N-1} \sum_{i}^{N} \left(\frac{O_i}{\sigma_i} \right)^2 \right]^{1/2}$$

where N is the number of observations, O_i is the ith observation, and σ_i is the ith standard error. The S/N for the triangulation data is 3.33. About 27% of the angle changes are equal to or smaller than the observation uncertainties. The low S/N is likely a function of the geometry of the network: the majority of the triangulation observations are within the upthrown block and do not span the 1952 surface rupture. Furthermore, the orientations of many of the observed triangles are not optimal for resolving deformation along the fault.

2.2. Leveling

The leveling data used in this study were collected by the USCGS [*Whitten*, 1955] and evaluated by *Stein and Thatcher* [1981] for slope-dependent and misclosure errors (Table 2a). The majority of the monuments were initially surveyed in 1926 and then resurveyed in 1953 following the mainshock. A small segment of the southern leveling line was surveyed in 1947 and

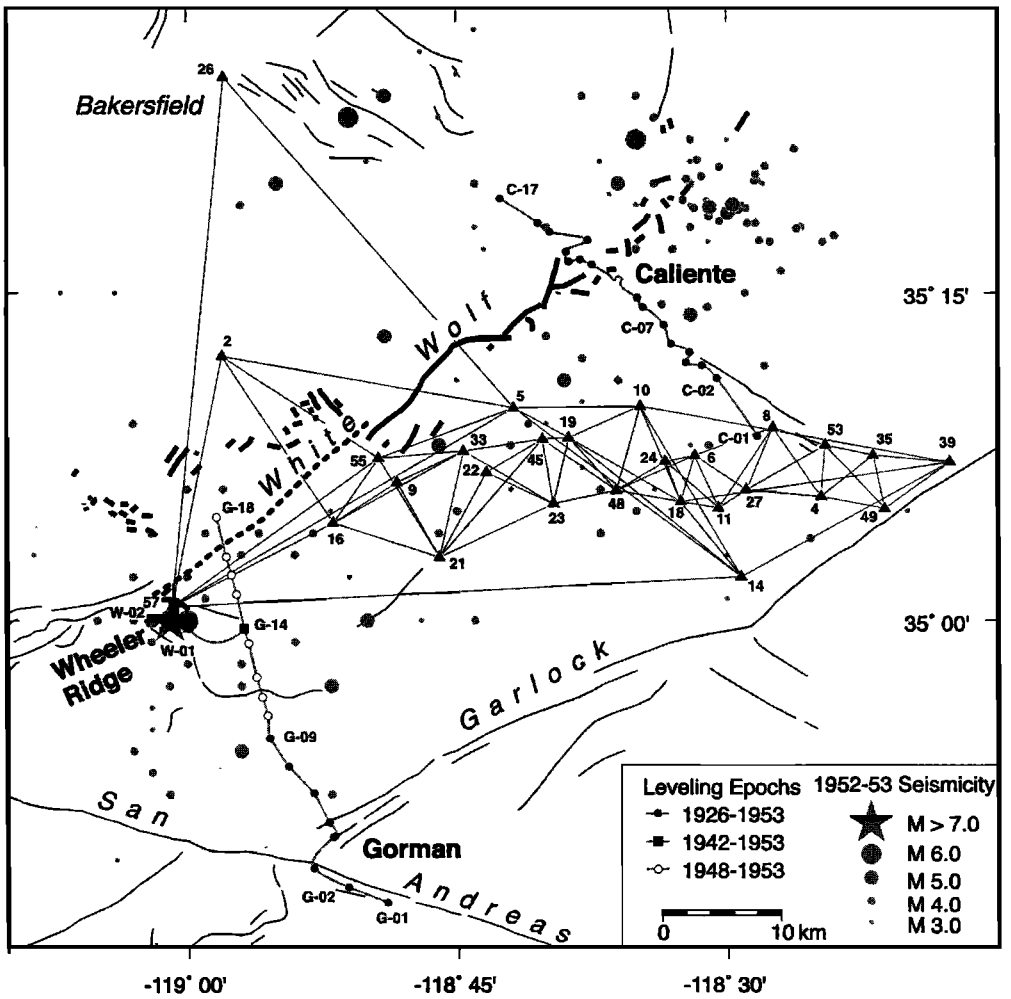

Figure 2. Geodetic network and seismicity, 1952–1953. The numbered triangulation stations (triangles) and leveling benchmarks (circles) correspond to observations in Tables 1 and 2. The 1952 surface ruptures are shown in bold black lines. Star, 1952 epicenter.

1953 (Figure 2). In the analysis, I use two primary leveling lines that span both the northern and southern end of the 1952 surface rupture, as well as the spur line (1948-1953) to the top of Wheeler Ridge near the 1952 epicenter (Figure 2). Most of the leveling monuments used in the inversions for all three lines are located on the hanging wall block of the White Wolf fault (Figure 1) and are less susceptible to possible nontectonic contamination from groundwater and hydrocarbon-related subsidence observed north of the White Wolf fault [*Lofgren*, 1975; *Stein and Thatcher*, 1981]. I use the elevation changes between successive benchmark pairs as the leveling observable, so that the observations are independent of elevation changes at the endpoints (Table 2b). The standard error for each segment is $\alpha\sqrt{L}$ in millimeters, where α is a constant based on the precision of the leveling survey set to 2.0 mm and L is the distance between monuments in kilometers. *Stein and Thatcher* [1981] furnish a complete description of the leveling uncertainties. The root-mean-square (rms) uncertainty of the leveling data is 4 mm with a S/N of 27.4. The combined rms S/N for both the triangulation and leveling data is 12.2.

3. Singular Value Decomposition

I use single-value decomposition [*Menke*, 1989] to estimate slip along the White Wolf fault and to evaluate where fault slip is well constrained (resolution) and to what limits the slip can be determined (uncertainty). I solve $\mathbf{d} = \mathbf{Am}$, where $\mathbf{A}$ is a partial derivative matrix that relates the observed data, $\mathbf{d}$ ($i = 1, m$) to the model parameters that I seek, $\mathbf{m}$ ($j = 1, m$). The model parameter m_k is either the dip-slip or strike-slip component of displacement on a rectangular fault segment. The $\mathbf{A}$ matrix can be decomposed to $\mathbf{A} = \mathbf{U\Lambda V}^{\mathbf{T}}$, where $\mathbf{U}$ is an $M \times J$ set of eigenvectors which span the data space, $\mathbf{V}$ is a $J \times M$ matrix of eigenvectors that span the model parameter space, and Λ is a diagonal matrix of singular values ordered by size [*Menke*, 1989]. The solution vector $\mathbf{m} = \mathbf{V}_p\Lambda_p^{-1}\mathbf{U}_p$ ranges from an a priori fixed model ($p = 0$) to the least squares solution ($p = M$), where p are the number of singular values used ($0 \le p \le M$) [*King and Thatcher*, 1998].

The model resolution matrix $\mathbf{R}$ quantifies how well the slip components are resolved along the fault segments [*Menke*, 1989]. Each row of the resolution matrix corresponds to one slip

Table 1a. Kern County Triangulation Stations

Number	Latitude, deg	Longitude, deg	Station
01	34.97693	-117.65200	ACROSS
02	35.20144	-117.03239	ADOBE
03	34.90006	-117.64121	BAJADA
04	35.09420	-117.58681	BED
05	35.16190	-117.30266	BLACK OAK
06	35.12565	-117.47012	BRITE
07	35.07204	-117.66608	CAMERON
08	35.14708	-117.54242	CHAPI
09	35.10517	-117.19454	COMMANCH
10	35.16332	-117.42014	CUB
11	35.08576	-117.49225	DEER
12	35.08553	-116.06091	DESERT
13	35.03949	-117.67960	DOLEMITE
14	35.03325	-117.51327	DOUBLE
15	35.27005	-118.57803	ELK
16	35.07448	-117.13563	EL PASO
17	34.88021	-117.69918	FAULT
18	35.09058	-117.45730	FENCE
19	35.13933	-117.35423	FLANNAGAN
20	34.96121	-117.71704	GOLD
21	35.04803	-117.23360	GORGE
22	35.11281	-117.27735	HORSETHIEF
23	35.08901	-117.33955	JACKS
24	35.12109	-117.44330	JAIL
25	34.84961	-117.63548	JOSHUA
26	35.41431	-117.03411	KERN
27	35.09958	-117.51794	KILN
28	34.95580	-117.42666	LIEBRE
29	35.01060	-117.63385	LIMESTONE
30	34.79750	-117.69263	LITTL270
31	34.79750	-117.69263	LITTLE B
32	34.80829	-117.63970	LOPE
33	35.12904	-117.25615	MART
34	34.35224	-117.57044	MAY
35	35.12598	-117.63456	MONOLITH
36	34.85209	-117.62957	MOVE
37	34.74566	-117.67492	NUMBER R
38	34.83214	-117.68483	OLD RESE
39	35.12074	-117.70544	PAJUELA
40	35.07763	-117.69385	PASS
41	34.92017	-118.59458	PELATO
42	34.56097	-117.64396	PELONA
43	35.05808	-117.60712	QUARTZ
44	34.98887	-117.67360	QUICK
45	35.13810	-117.32969	ROCK SPRINGS
46	34.80498	-117.64746	SAND
47	34.69314	-117.43861	SAWMILL
48	35.09913	-117.39790	SCHOOL
49	35.08543	-117.64567	SHRUB 2
50	34.86327	-117.67350	SINGLE 2
51	34.98251	-117.81116	SOLEDAD
52	34.91282	-117.69998	STRAIGHT
53	35.13365	-117.59064	SUMMIT
54	34.93639	-117.69052	T10N R14
55	35.12379	-117.17744	TEJON228
56	34.94562	-117.64670	WASH
57	35.01059	-118.98572	WHEEL250

component for a given fault segment. As p increases from 0 to M, the fault segments that are resolved best have maximum values along the diagonal of **R**, while unresolved slip parameters in other rows in the matrix remain small. When $p = M$, **R** is the identity matrix and all of the parameters are uniquely resolved, the least squares inversion. Typically, as p increases, the model fit improves to the point where additional eigenvalues do not significantly improve the model fit. An F test is used here to assess whether the improvement in the model fit justifies increasing the number of singular values. Once there is little improvement in the model fit, the rows of **R** with the largest diagonal elements represent the slip components on the fault segments that are best resolved. The rows of **R** that are poorly resolved need to be reassessed, excluded from the inversion, combined with neighboring segments, or constrained by additional data. Once these poorly resolved segments have been addressed, the final step involves a least squares inversion where each of the model parameters will be uniquely resolved.

The single-value decomposition method of treating the geodetic data differs from previous coseismic geodetic studies [*Dunbar et al.*, 1980; *Stein and Thatcher*, 1981] by directly modeling each angle change as a discrete observation, instead of forward modeling the derived components of shear strain by groups of 3-4 monuments. I use direct observation: no points need to be fixed or constrained to calculate the coseismic angle changes. Thus assumptions that apply to shear strain calculations, such as uniform shear within a network, no network dilation, and no network rotation, are avoided. Furthermore, by modeling the leveling data as relative elevation changes between adjacent monuments, errors associated with datum offsets between the preseismic and postseismic surveys are averted. However, since the covariance between successive monument pairs is not utilized, then the S/N for the leveling data may be overestimated. Another difference between this study and previous analyses is that I include additional triangulation data both north and south of the surface rupture.

4. Coseismic Fault Model

Determination of the coseismic fault model proceeded in a multistep process. First, an overparameterized fault model was constructed to examine where slip could be resolved both along the length of the fault and at depth. Second, the dip of the overparameterized fault model was varied over a wide range of values to evaluate how well the network can resolve variations in dip. Third, based on where the geodetic network could resolve slip, the fault model was reparameterized into a four-segment fault. Model parameters were then incrementally varied to determine the fault geometry (endpoint location, dips, and fault depths). Fourth, the model resolution was then reevaluated, resulting in a further reparameterization of the fault into two segments. I again used a grid search on the two-segment model to determine the geometry of the preferred model. Finally, the data were inverted to determine the coseismic slip distribution.

4.1. Model Resolution

To evaluate the resolution of the triangulation and leveling data on the fault plane, a fault plane with a dip of 75°, the steepest dip suggested for the White Wolf fault, was divided into 30 patches (ten 6.6-km patches along strike and three 5-km patches down dip) (Figure 3a). This overparameterized fault model was not used to estimate slip; rather, it was used to examine where on the modeled fault surface the data could resolve slip and, more importantly, where the resolution is poor. Figure 4 shows how the model fit varies as the number of singular values increases. The approach used here is to find the turning point in the trade-off curve of the model fit versus the number of singular values [e.g., *Harris and Segall*, 1987]. The model fit improves rapidly for the first nine singular values and then improves more slowly. After 29 singular values, the model fit levels off, suggesting that there is little gain with additional parameters. Evaluating the resolution at the 29th singular value, I found that the data best resolves shallow (0-5 km deep) slip along

Table 1b. The 1951-1953 White Wolf Fault Angle Changes[a]

Triangle			Δθ,	Triangle			Δθ,
A	V	B	s	A	V	B	s
05	02	57	7.36	16	21	55	-7.84
16	02	57	4.88	22	21	45	0.93
27	04	53	0.54	33	21	22	0.87
49	04	27	0.70	23	22	21	-9.66
53	04	35	-1.39	45	22	21	-2.43
53	04	49	0.91	45	22	23	6.98
10	05	14	3.41	19	23	48	-1.42
10	05	19	2.41	22	23	19	-3.97
19	05	14	1.23	22	23	45	-0.84
55	05	02	-5.71	33	23	19	-2.93
57	05	55	-1.08	33	23	45	-1.18
08	06	11	1.76	33	23	48	-4.51
08	06	18	3.38	45	23	19	-3.08
08	06	27	3.47	06	24	11	-1.67
08	06	48	-1.80	06	24	18	1.08
11	06	18	1.65	06	24	48	-4.68
18	06	48	-5.18	11	24	18	2.75
27	06	11	-1.10	18	24	48	-5.82
48	06	24	1.94	05	26	57	4.12
04	08	27	1.68	06	27	08	-6.80
11	08	06	1.44	53	27	04	2.31
27	08	11	0.67	09	33	55	-3.74
53	08	06	2.41	16	33	09	-1.58
53	08	11	0.97	21	33	16	1.93
53	08	27	1.36	23	33	21	-8.87
21	09	16	4.04	45	33	21	-5.51
33	09	16	5.22	45	33	23	1.45
33	09	21	1.96	04	35	53	1.15
14	10	18	1.61	53	35	39	-1.72
18	10	48	-6.59	18	39	35	-0.85
19	10	05	1.01	49	39	35	0.87
39	10	05	-4.19	19	45	23	3.13
39	10	18	2.01	19	45	48	3.91
39	10	19	-5.54	21	45	22	1.64
39	10	48	-5.04	22	45	33	1.52
48	10	19	-0.70	23	45	21	-4.43
06	11	08	-4.49	48	45	23	-0.78
06	11	27	-1.55	06	48	18	2.19
08	11	27	2.48	10	48	24	0.66
18	11	06	-1.28	18	48	23	-4.6
18	11	08	-5.18	19	48	10	-7.30
18	11	24	-1.16	23	48	06	2.04
18	11	27	-2.83	23	48	19	7.64
05	14	19	0.53	23	48	24	1.54
18	14	10	3.76	23	48	45	4.78
19	14	18	-4.35	24	48	06	0.28
19	14	39	-4.95	45	48	19	2.85
57	14	19	6.24	04	49	53	0.66
02	16	55	0.77	53	49	35	0.95
09	16	33	-3.09	04	53	27	-1.17
21	16	57	7.81	08	53	35	0.42
33	16	21	-3.86	27	53	08	1.49
55	16	09	2.96	35	53	27	-1.91
55	16	33	0.70	35	53	49	-0.28
57	16	02	-5.42	49	53	04	0.40
57	16	09	-3.33	02	55	05	5.27
57	16	33	-4.21	05	55	21	-8.96
57	16	55	-5.53	05	55	33	-5.99
10	18	24	-1.54	05	55	57	1.72
14	18	19	0.78	16	55	57	2.28
19	18	39	-5.87	21	55	16	8.01
05	19	10	-4.73	33	55	21	-2.97
10	19	14	8.54	57	55	02	-6.70
10	19	18	9.08	02	57	16	0.65
10	19	23	3.21	02	57	55	-0.76
10	19	48	10.17	05	57	14	1.06
18	19	14	-0.62	05	57	16	1.25
23	19	45	-0.05	26	57	02	-0.66
45	19	05	1.46	26	57	05	-0.98
45	19	10	-3.16	55	57	05	-0.82
48	19	23	-6.96	55	21	09	7.70[b]

[a]A,V, and B are triangle vertices, where V is the observation point; Δθ is the angle change clockwise from AV to BV.

[b]Rejected observation.

Table 2a. Kern County Leveling Stations

Station	Latitude, deg	Longitude, deg
T 55	35.29028	-118.62833
U 55	35.28138	-118.64833
V 55	35.27361	-118.64583
1732 USGS[a]	35.27527	-118.63527
W 55	35.27138	-118.62416
Y 55	35.24639	-118.58222
2410 USGS	35.23889	-118.57694
Z 55	35.22556	-118.55806
2719 USGS	35.21083	-118.55138
A 56	35.20472	-118.53417
3064 USGS	35.19694	-118.53750
B 56	35.19444	-118.52278
C 56	35.18472	-118.50889
A 54	34.78417	-118.81556
B 54	34.79583	-118.85167
C 54	34.81027	-118.88361
D 54	34.83500	-118.86417
F 54	34.84528	-118.86972
G 54	34.86777	-118.88333
H 54	34.88806	-118.90667
K 54	34.92722	-118.92583
T 824	34.94111	-118.93028
M 54	34.95639	-118.93556
N 54	34.98222	-118.94278
S 604	34.99389	-118.94694
E 608	35.02000	-118.95444
P 64	35.03472	-118.95889
R 824	35.04861	-118.96361
S 604	34.99389	-118.94694
V 604	34.99444	-118.99972
Q 55	35.32166	-118.70944
R 55	35.30305	-118.67416
S 55	35.29638	-118.66333

[a]USGS, U.S. Geological Survey.

most of the surface trace of the fault (Figures 3b and c). Shallow dip slip can be resolved along both the epicentral and northeast ends of the fault, but is poorly resolved in the central portion of the fault. This is also true to a lesser extent for moderate depths (5-10 km) along the fault plane. Deep dip slip (10-15 km) can only be resolved on two segments near the southwestern end of the fault (resolution of ≥0.4). The ability of the data to resolve dip slip is primarily controlled by the location of the leveling routes and, to a lesser extent, the triangulation stations in the central region of the fault.

Strike slip is best resolved for shallow (0.0-5.0 km) displacements along the central 45 km of the fault (Figure 3c), the result of the high density of triangulation stations in the hanging wall. The resolution for the epicentral end of the fault is the product of the fault-crossing triangulation stations and the leveling line (Figure 3a). The lack of geodetic control at the northeastern end of the fault trace limits the ability to resolve slip in this region. The geometry of the network also allows minimal strike-slip resolution at moderate (5 to 10 km) and deep (10 to 15 km) portions of the White Wolf fault.

Since the surface rupture was poorly expressed and the aftershock locations have large uncertainties, the dip of the rupture plane is uncertain. Previous geodetic models of coseismic slip have found a variety of dips for the rupture plane(s) that range from 20° to 75° [*Dunbar et al.*, 1980; *Stein and Thatcher*, 1981], aftershock and seismicity studies find dips between 50° and 75° [*Cisternas*, 1963; *Ross*, 1986; *Castillo and Zoback*, 1995], focal mechanism studies find dips between 60° and 66° [*Gutenberg*, 1955], and seismic profiling yielded dips between 60° and 65° [*Goodman and Malin*, 1992]. To evaluate the ability of the network to resolve slip at various dips, I varied the dip of the 30-segment resolution model in 10° increments between 25° and 85°. Changes in the dip of the fault only slightly change the spatial resolution described above for the 75° dipping fault in Figure 3. Gently dipping fault planes tended to increase the ability to resolve nearer-surface (0-5 km) dip slip in the center of the fault, while decreasing the dip-slip resolution at depths greater than 5 km. For nearer-surface strike-slip displacement, gently dipping faults have a modest boost in resolution at either end of the fault plane. This pattern is also observed at moderate depths (5-10 km) and along the southwestern 15 km at greater depths. The geometry of the geodetic network can adequately resolve shallow strike slip and dip slip along the length of the fault and at a variety of dips, with the exception of the last 6-km at either end of the fault. The network can resolve moderate to deep dip slip below the leveling lines but lacks resolution along the central portion of the fault.

4.2. Fault Geometry

To determine the geometry and fault model parameters to be used in the preferred inversion, I used a grid search method that incrementally varied each parameter while minimizing the reduced chi square (χ^2) in a joint inversion of the leveling and triangulation observations. Each iteration solved for both the

Table 2b. Elevation Changes

From	To	Elevation Change, cm	σ
C-01	C-02	3.42	0.33
C-02	C-03	1.06	0.33
C-03	C-04	2.75	0.33
C-04	C-05	-1.25	0.33
C-05	C-06	2.38	0.33
C-06	C-07	0.12	0.36
C-07	C-08	4.47	0.33
C-08	C-09	-0.43	0.56
C-09	C-10	-7.71	0.33
C-10	C-11	-14.01	0.33
C-11	C-12	-11.20	0.33
C-12	C-13	2.89	0.38
C-13	C-14	15.54	0.38
C-14	C-15	-13.02	0.38
C-15	C-16	7.28	0.33
C-16	C-17	7.22	0.41
G-01	G-02	1.61	0.40
G-02	G-03	2.59	0.40
G-03	G-04	1.04	0.38
G-05	G-06	3.38	0.33
G-06	G-07	4.85	0.34
G-07	G-08	5.00	0.38
G-08	G-09	7.00	0.36
G-10	G-11	6.49	0.33
G-11	G-12	6.02	0.33
G-12	G-13	5.87	0.34
G-13	G-14	-1.38	0.33
G-14	G-15	-5.61	0.34
G-15	G-16	-9.85	0.33
G-16	G-17	-15.56	0.33
G-17	G-18	-37.09	0.38
G-14	W-01	3.82	0.46
W-01	W-02	-14.42	0.38

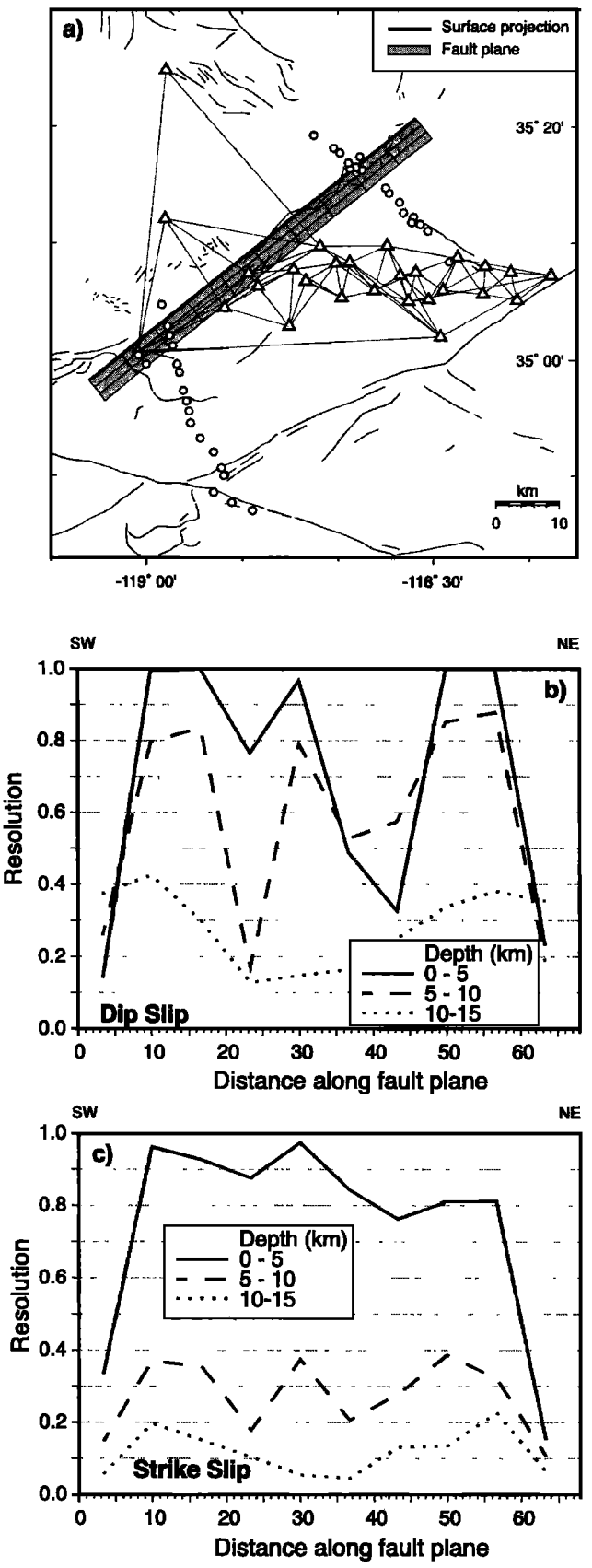

Figure 3. (a) Geometry of the resolution model to the geodetic network; (b) dip-slip resolution and (c) strike-slip resolution as a function of depth along the White Wolf faults. Solid lines are for depths of 0-5 km, dashed lines are 5-10 km, and dotted lines are 10-15 km.

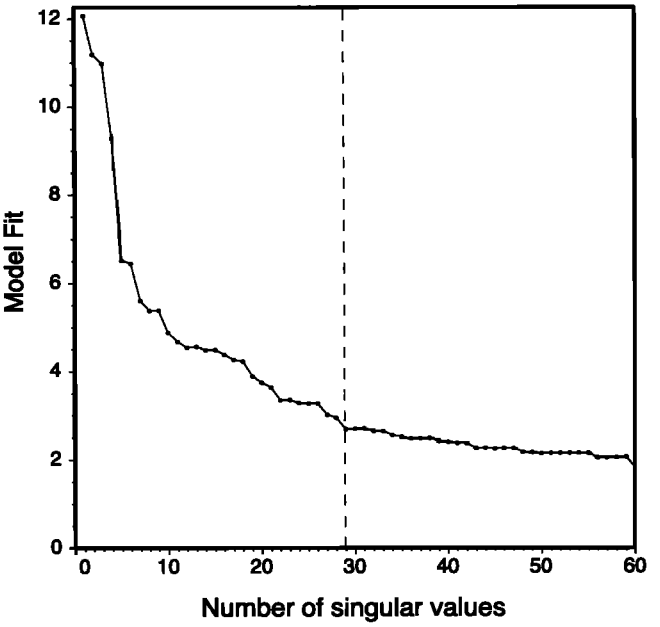

Figure 4. Model fit (reduced χ^2) versus the number of singular values. The dashed line represents the point at which there is little improvement in the model fit with additional eigenvalues.

stirke- and dip-slip components on each fault segment. The χ^2 is computed as

$$\chi^2 = \left[\frac{1}{N-N_f}\sum_i^N\left(\frac{O_i - C_i}{\sigma_i}\right)^2\right]^{1/2},$$

where N is the number of observations, N_f is the number of free model parameters, O_i is the ith observation, and C_i is the ith calculated elevation change. I began with a four-segment version of the resolution fault model and changed the dip on each fault plane in 5° increments between 25° and 85° for a total of 20,736 iterations. I found that the models with the lowest χ^2 had dips between 65° and 85°. On the basis of this observation, I constrained the dip of each fault segment to 75°, thereby lowering the number of free model parameters.

I used the aftershock distribution and reduced chi square to determine the fault plane depths (depth is defined as the vertical elevation below the surface). The Kern County earthquake aftershocks and recent seismicity show a bimodal distribution of earthquake depths along strike, with deeper seismicity (<25 km) near the epicentral region to the southwest and shallow events (<10 km) in the northeast [*Gutenberg*, 1955; *Castillo and Zoback*, 1995; *Bawden et al.*, 1999]. Since the network can resolve deeper slip (Figure 3) and the seismicity suggests deeper coseismic slip in the southwest, I initially set the downdip depth of the epicentral patch to 20 km and similarly set the maximum depth at 10 km for the northeastern segments. Incrementally adjusting both the minimum and maximum depths in 0.5-km steps for each fault segment and evaluating the χ^2, the southwestern fault segments had the lowest χ^2, with upper depths of ≥6.0 km and lower depths of >27 km. The χ^2 continued to decrease with both deeper minimum and maximum fault depths, but since the rate of improved model fit was lower at increasing depths and because of the inability to distinguish deep slip, these values were used in the inversion. Using a similar rationale, the northeastern fault segments had low χ^2 with minimum depths of

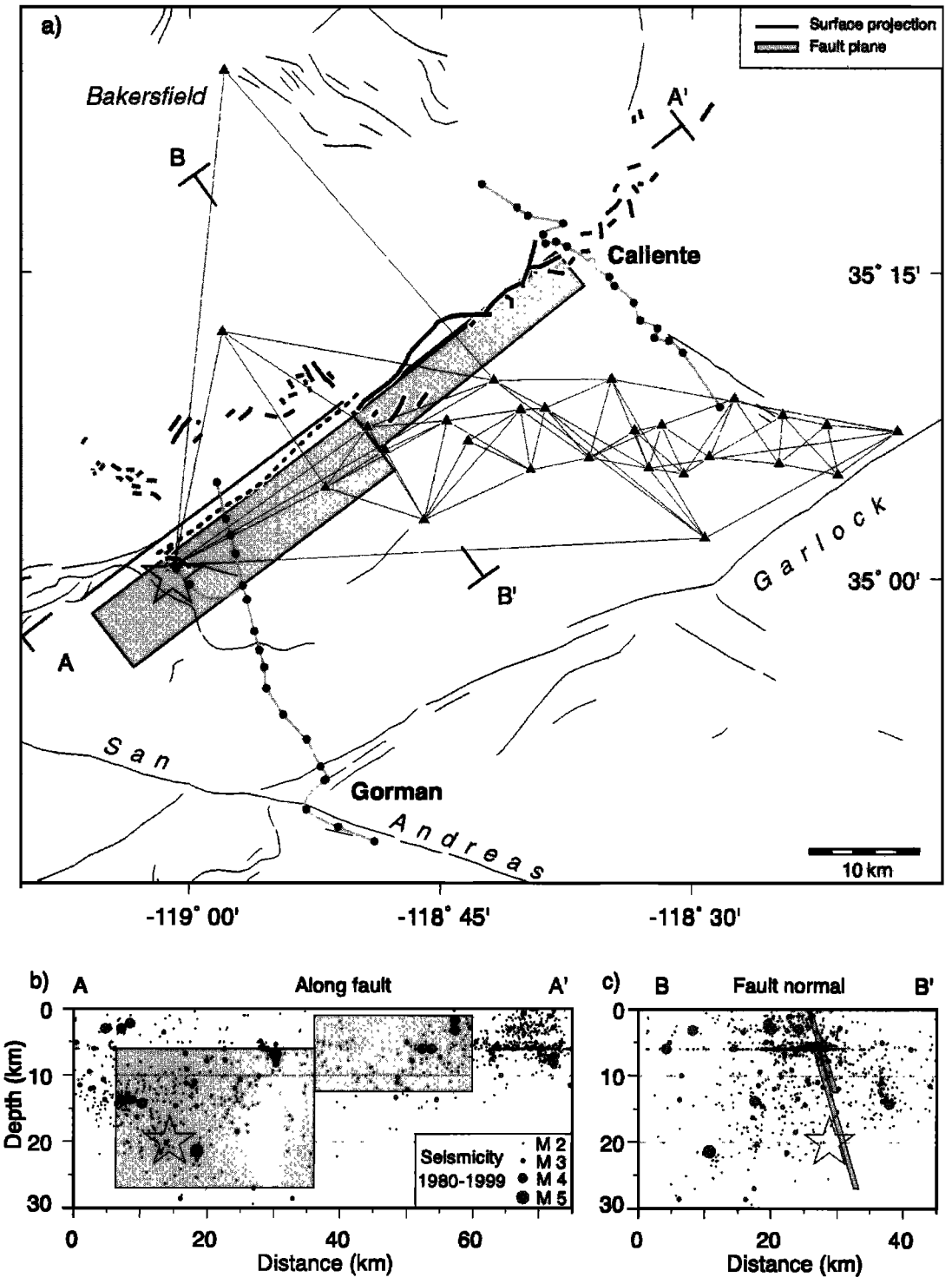

Figure 5. (a) Geometry of the preferred fault model to the geodetic network, (b) along-fault seismicity (1980-1999), and (c) fault normal seismicity. Bold lines associated with the fault model are the surface project of the fault plane. Star, 1952 epicenter; triangles, triangulation stations; circles, leveling benchmarks.

near 1.0 km and a maximum depth of 12.5 km. Therefore both fault depths were determined by the geodetic data, with the maximum depth of the epicenteral patch partly constrained by the seismicity.

To determine the coordinates of the fault endpoints, I minimized the χ^2 for joint inversions of the triangulation and leveling data carrying out a grid search of the fault position, varying the latitude and longitude in 0.002° increments (about 220 m) over a 0.10° range (11 km). The strike of each segment was constrained at 51° (the average strike of the surface trace of the White Wolf fault), and the segments were not allowed to overlap or separate along strike. The models with the lowest χ^2 values shifted the fault segments to the southwest along the White Wolf fault. The placement of the northeastern fault patch is strongly controlled by leveling data, with poor resolving capability northeast of the leveling line. The data are insensitive

Table 3. Fault Model Parameters

Parameters	Southwest	Northeast
Strike, deg	51	51
Dip, deg	75	75
Length, km	29.7	23.6
Upper depth, km	6	1
Lower depth, km	27	12.5
Latitude Npt[a]	35.132	35.265
Longitude Npt	-118.840	-118.636
Latitude Spt	34.970	35.132
Longitude Spt	-119.100	-118.840

[a]Npt, northern endpoint of fault; Spt, southern endpoint of fault.

to extension of the epicentral fault patch to the southwest. From this, the fault was resized and partitioned into two patches of equal length and a new set of inversions was performed to determine their position while minimizing the χ^2. The endpoints were allowed to incrementally move, in 0.10° and 0.5-km increments (position and depth), but the strike was constrained at 51° and again the fault patches were not allowed to overlap or separate. The geometry of the preferred fault model is shown in Figure 5 and Table 3 and is in good agreement with the present-day microseismicity. A comparison of the *Goodman and Malin* [1992] fault map, determined by geological mapping, well log data, and deep crustal seismic profiles, with the geodetically derived fault model shows an excellent agreement of the fault geometries, including the right-stepping jog approximately midway along the fault (Figure 6).

5. Coseismic Slip Distribution

The coseismic slip distribution was determined by first inverting the triangulation data to obtain the coseismic strike-slip displacements and then fixing these values while inverting the leveling data for the dip-slip components. This approach was necessary because the low S/N of the triangulation relative to the leveling data placed an inordinate weight on leveling observations during the joint inversion. This resulted in slip models inconsistent with observed coseismic offset patterns (Table 4). The preferred model, which is, of course, not the only possible model, fits the leveling data well along all three profiles (Figure 7). The offset of the Wheeler Ridge spur line to the west from the Highway 99 line (Figures 7a and b) provided needed constraints on the geometry of the fault model, because minor changes in the geometry would result in large reduced chi square values in these lines. Similarly, lateral variations in the monument spacing along the Caliente leveling line, which followed a winding road somewhat perpendicular to the surface rupture (Figure 1), resulted in an "apparent scatter" of the data (Figure 7c, e.g., between 10 and 25 km) or unusual uplift patterns (Figure 7d, e.g., between 40 and 50 km). This apparent scatter is in part due to the lateral vertical deformation gradient and was useful in determining the fault geometry for the northeastern fault segment. This preferred model places 3.6 m of left-lateral strike slip and 1.6 m of reverse slip on the southwestern segment (Table 4 and Figure 7). Left-lateral strike slip decreases in the northeast to 0.2 m, with 1.7 m of reverse slip. The χ^2 value decreases from 12.16 to 3.48 (Table 4).

Since the χ^2 values are greater than 1.0, the model does not satisfy all of the data to within their uncertainties (a perfect fit corresponds to a reduced chi square of 1.0). The preferred model explains 96% of the leveling data, but only 49% of the triangulation data. The reason for the modest reduction in the reduced chi square for the triangulation is unclear. The misfit is scattered fairly evenly throughout the network except at the eastern end where the data are satisfied at or near the data uncertainty (Figure 8). One possibility is that since there are only 16 closed triangles to assess the data quality, I have underestimated the data uncertainties for the network. One possible implication of $\chi^2 > 1$ in the preferred model is that assigned uncertainties to the slip model are underestimated. I account for this shortcoming by recomputing the slip uncertainties by multiplying the formal slip uncertainty by the square root of the reduced χ^2 value [*Thatcher et al.*, 1997]. These larger uncertainties are listed in Table 4 and are specific to the fault geometry of the preferred model.

Given that the leveling observations have a high signal-to-noise ratio and that the locations of the three leveling lines cross both of the fault ends, the leveling data alone were inverted to estimate slip (Table 4). The distribution of the coseismic slip in the southwest is similar to the joint inversion at the 2σ confidence level with 3.8 m of left-lateral strike slip and 1.6 m of reverse slip. However, the models differ for the northeastern segment. The leveling-only model produced 4 times (0.9 m) the amount of left-lateral strike slip than the combined triangulation/leveling inversion, with only minor increase in the reverse slip (2.0 m) (Table 4).

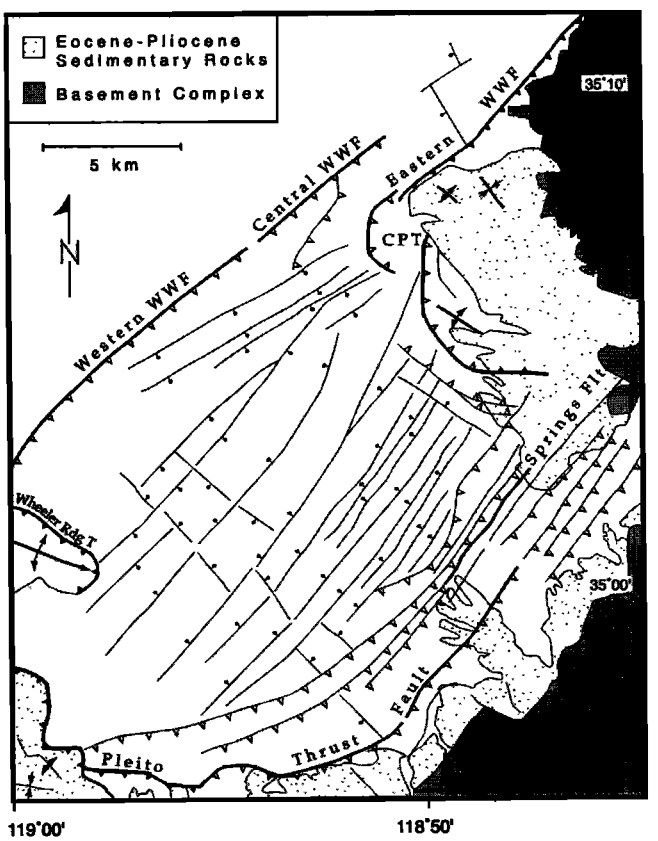

Figure 6. Detailed fault map of the central White Wolf fault. The bold faults and folds are active structures [*Goodman and Malin*, 1992]. Barbs represent exposed thrusts (solid barbs) and blind thrusts (open barbs). CPT, Comanche Point thrust; Rdg., Ridge; WWF, White Wolf fault. Modified from *Goodman and Malin* [1992].

Table 4. Model Misfits

Model	Signal to Noise	Misfit to Noise	Percent Signal Explained[a]	Southwest Segment		Northeast Segment	
				Reverse Slip, m	Left-Lateral Strike Slip, m	Reverse Slip, m	Left-Lateral Strike Slip, m
Triangulation	3.33	2.83	49	...	3.56 ± 0.28	...	0.18 ± 0.13
Leveling -dip slip only	27.39	7.15	93	1.64 ± 0.03	...	1.61 ± 0.04	...
Leveling	27.39	5.37	97	1.60 ± 0.03	3.81 ± 0.35	2.02 ± 0.11	0.88 ± 0.25
Joint Trig and Leveling	12.16	4.15	52	1.62 ± 0.03	3.64 ± 0.23	1.39 ± 0.05	-0.31 ± 0.11
Preferred Model	12.16	3.48	69	1.63 ± 0.03	3.56 ± 0.32	1.89 ± 0.04	0.22 ± 0.14

[a]Reduction in the misfit-to-noise ratio.

Is there a significant difference in the reduction of residuals between the inversion of leveling only and the joint inversion? To address this question, I compared the misfits of the two models with an F test:

$$F = \left[v_1 \sum_{k=1}^{N_1} r_k^2 / \sigma_k^2 \right] \Big/ \left[v_2 \sum_{i=1}^{N_2} r_i^2 / \sigma_i^2 \right],$$

where r is the residual (observed minus calculated); σ is the data uncertainty; and v_1, v_2 are the number of degrees of freedom for models 1 and 2, respectively. The joint inversion produced F = 2.56, which is significant at the 99% confidence level. Thus the combined leveling and triangulation inversion provides a better fit to the data, even though the model reduced the triangulation signal by only 49%.

The geodetic moment was calculated for the Kern County earthquake from the preferred model (Table 5) by using

$$M_o = \mu \sum_{i=1}^{4} A_i S_i ,$$

where $\mu = 3 \times 10^{10}$ N/m^2 is rigidity, and A_i and S_i are the area and slip estimated from fault segment i, respectively. This yields M_o = (9.2 ± 0.5) × 10^{19} N m (M_W of 7.22), in good agreement with results from other seismic and geodetic studies (Table 5).

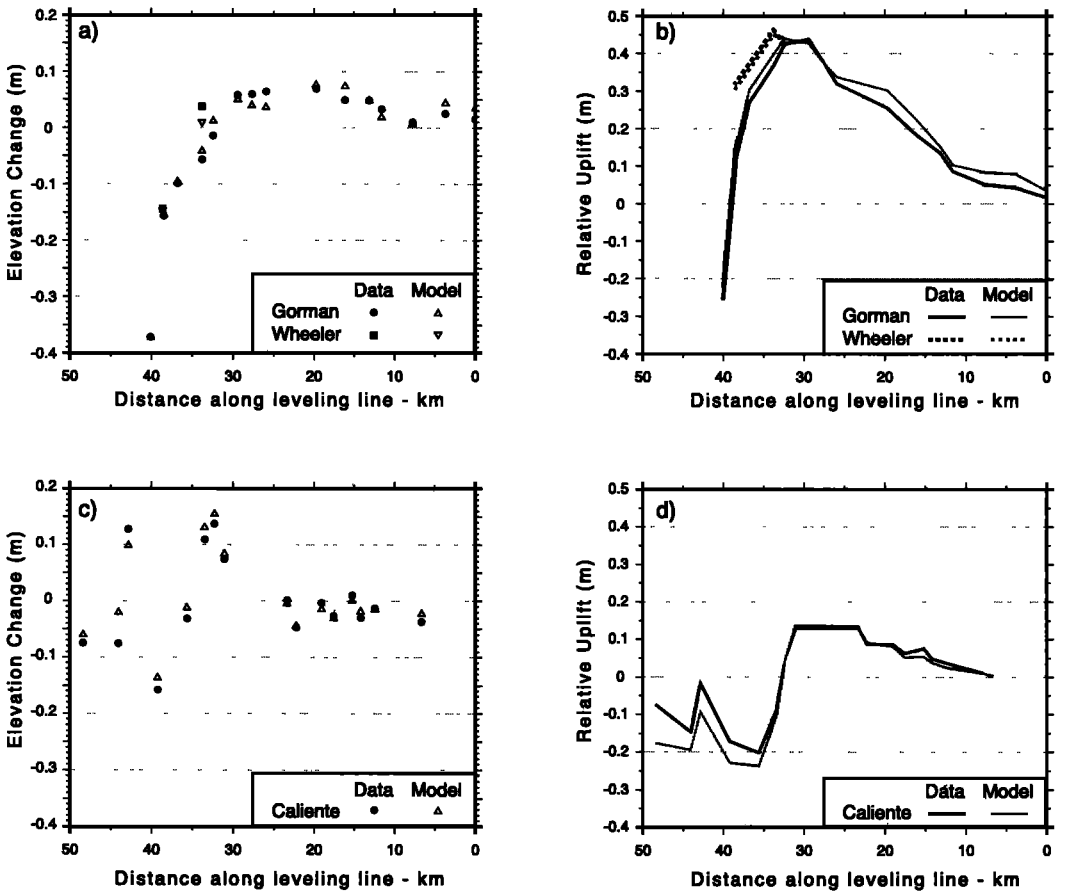

Figure 7. Coseismic and modeled elevation changes for the (a, b) Highway 99 and Wheeler Ridge spur and (c, d) Caliente leveling lines. Elevation change is the coseismic change in height between adjacent leveling monuments. Relative uplift is the sum of the elevation changes along leveling line starting at the southernmost leveling point and represents the coseismic uplift pattern along the leveling profile.

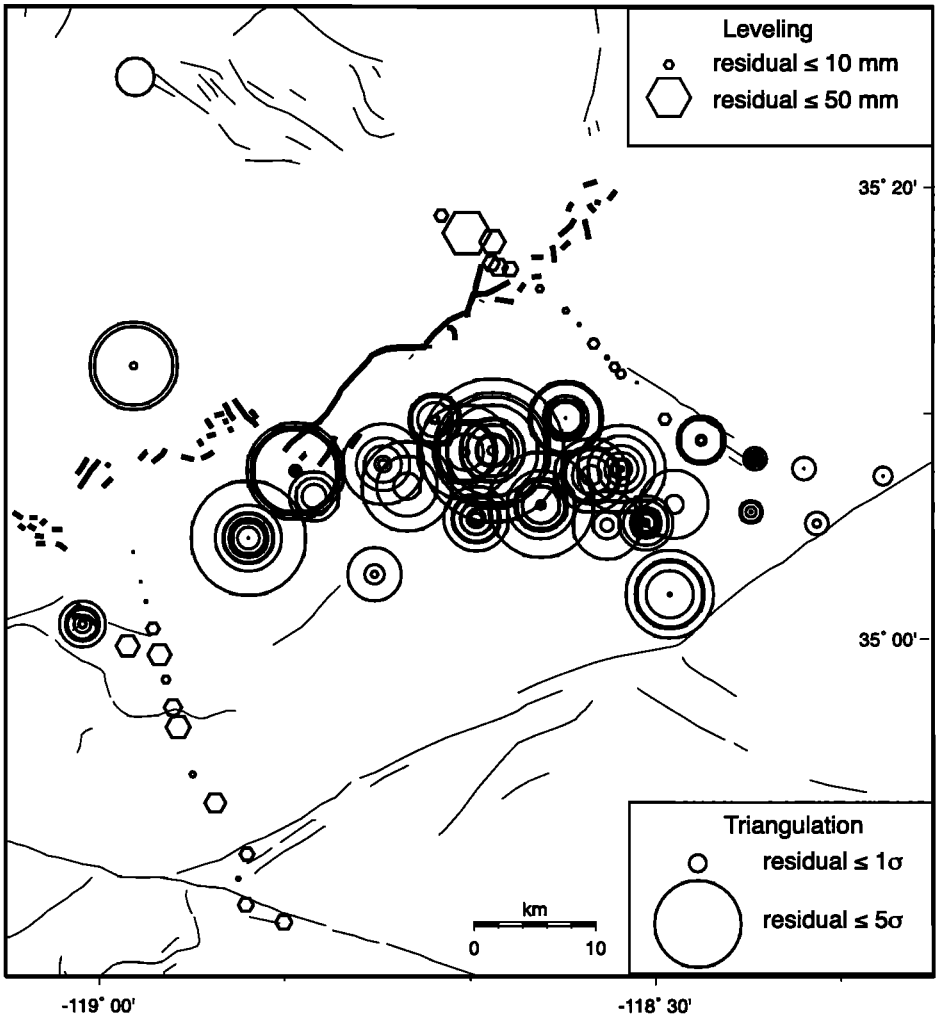

Figure 8. Residual triangulation and leveling signal from the inversion. Circles, triangulation residuals normalized by their uncertainty for each observation. Each circle represents the residual for a given angle change measured at the monument represented by the circle. Small circles represent a good match between the model and the observation. Hexagons, residual elevation changes in millimeters.

6. Discussion

6.1. Data Misfit

Since none of the fault models that I tested completely replicated the signal to within the observational uncertainty, some aspect of the faulting behavior remains unmodeled. There are a number of possibilities to explain the model's inability to explain the entire signal. The preferred model may be an oversimplified approximation of the true fault geometry. Unfortunately, the data available will not allow us to explore models with added complexities. Another explanation for the unmodeled signal may lie with the modeling assumptions. I assume uniform-slip faults in an isotropic, homogenous elastic media. Additional segmentation of the fault model with subsequent inversions suggests that the largest of strike-slip displacement occurred in the central region of the fault. However, this model is not significant at the 99% confidence level owing to the added number of free parameters for the additional fault planes. The assumption of an isotropic and homogenous medium is also not realistic along the White Wolf fault. The geology varies both along fault and cross fault with a complex mixture of southern Sierra Nevada basement rock and basin sediments (Figure 1) [e.g., *Goodman and Malin*, 1992].

Alternatively, the modeled misfit may be a product of nontectonic or secondary deformation that locally disturbed the network or, may reflect complexities associated with oblique-reverse fault earthquakes. The most notable source of nontectonic deformation is from groundwater-related subsidence in the southern San Joaquin valley [*Lofgren*, 1975; *Stein and Thatcher*, 1981; *Bawden et al.*, 1997]. To minimize this source of contamination, leveling monuments selected were located in the hanging wall of the White Wolf fault, placed in bedrock, had shallow depths to bedrock, or were surveyed close in time to the mainshock (Figures 1 and 2). Since the triangulation observations were taken within 6 months of the mainshock, then the horizontal component of any signal other than the coseismic should be much lower than the uncertainties associated with the measurements. Triggered slip on smaller faults or local monument instabilities, such as those induced from ground shaking, would also have similar effect. Three aftershocks $M_L \geq 6.1$ located near the network (Figure 2) may have introduced local movement at a few of the monuments. In particular, station

57 on Wheeler Ridge was within 2 km of a M_L 6.4 aftershock (Figure 2).

6.2. Comparison With Other Studies

The geometry and the slip distribution from the preferred model differ significantly from previous geodetic analysis that used forward modeling techniques (Figure 9 and Table 5). One of the most apparent differences among the three geodetic models is the spatial geometry of the fault planes. The *Dunbar et al.* [1980] model is a straight fault that approximates the endpoints of the primary surface rupture and is divided into two shallow and two deep patches (Figure 9b and Table 5). The differences between the *Dunbar et al.* [1980] model and the model here in are that I find a right-stepping jog approximately midway along the fault and the fault is shorter. Additionally, the data are insufficient to resolve slip on multiple downdip patches, as well as along the entire length of the northeastern fault patches. The *Stein and Thatcher* [1981] three-segment, curvilinear fault model poorly matches the surface rupture trace of the White Wolf fault and extends well beyond the resolving capabilities of the geodetic data to the northeast (Figure 9c). Inversions that only included triangulation data tended to have a southwestern fault segment with an easterly orientation, similar to the work of *Stein and Thatcher* [1981]. However, these more easterly trending fault segments failed to satisfy the leveling data, in particular, the spur leveling line on Wheeler Ridge that was not used in their modeling (Figure 2).

Another difference in the fault models is the dip of the northeastern fault segment. The *Dunbar et al.* [1980] model uses a constant dip of 65°, while the *Stein and Thatcher* [1981] model has a decreasing dip from 75° in the epicenteral region to 20° at the northeastern end (Table 5). The inversion found that a uniform dip of 75° to the southeast explains the leveling data best. More gently dipping (<60°) fault planes failed to match the elevation changes along the northern leveling line and were rejected. It is unclear why the dip for the northeastern fault segment varies so much between the *Stein and Thatcher* [1981] model and the preferred model. I omitted leveling data that may have been subjected to subsidence associated with groundwater or hydrocarbon pumping north of the White Wolf fault and monuments with questionable stability near Tehachapi (Figure 9). The exclusion of these data provided a more robust solution with fewer potential sources of nontectonic contamination. These data omissions may be one of the reasons that the preferred model differs from the *Stein and Thatcher* [1981] model. Additionally, since the northern fault patch on their model extends well beyond the resolution capabilities of the geodetic array (Figure 9), the slip and geometry of this fault patch are unreliable.

Another difference among the three geodetic models is the slip partitioning along the fault surfaces. I found a nearly uniform reverse slip along the fault, while other geodetic studies

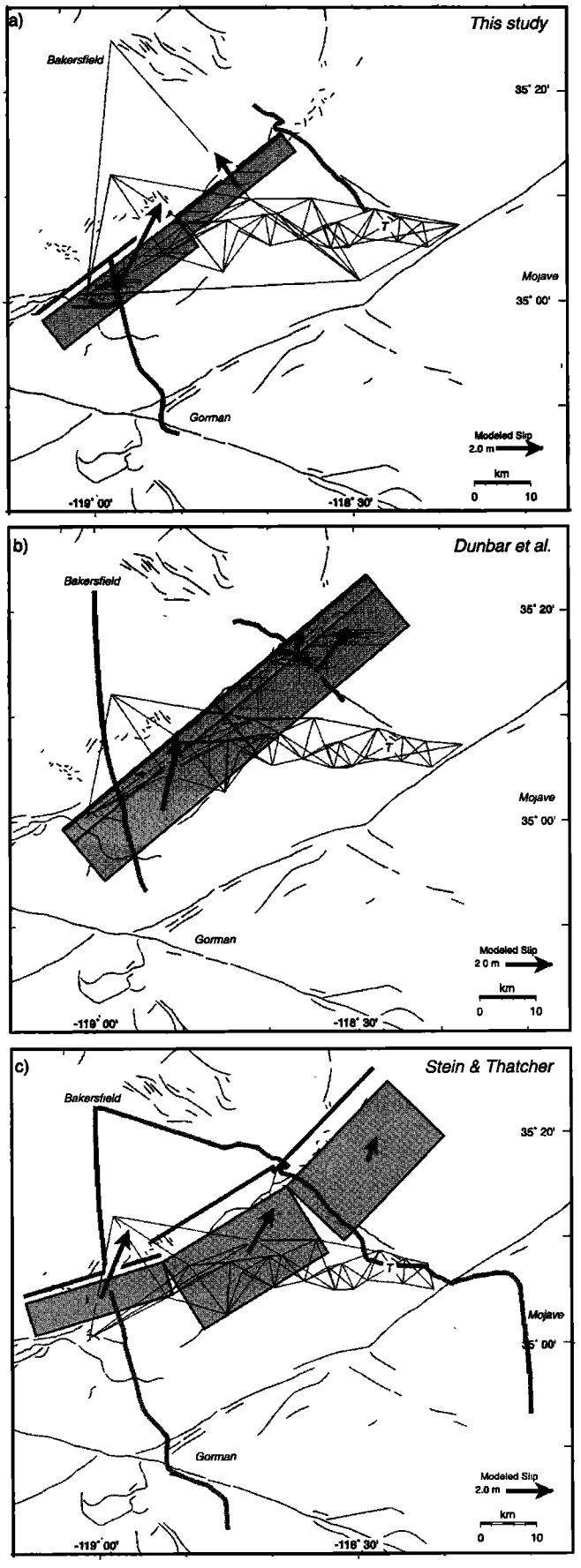

Figure 9. Comparison of geodetic models from (a) this study, (b) *Dunbar et al.* [1980], and (c) *Stein and Thatcher* [1981]. The bold gray lines are the leveling segments used, and the thin black lines are the triangulation measurements used in each study. The fault coordinates for Figures 9b and 9c are approximate. T, Tehachapi.

Table 5. Source Studies

Reference	Data Type	Fault Segment	Strike, deg	Dip, deg	Length, km	*Hmin*, km (Depth, km)	*Hmax*, km (Rake, deg)	Reverse Slip, m	Left-Lateral Strike Slip, m	Moment, 10^{19} N m
Gutenberg [1955]	first motion		050	60-66 E		(18-20)	(54)			20
Hanks et al. [1975]	isoseismal									$M_w = 7.50$
Kanamori	S wave									17
unpublished data	spectra									$M_w = 7.45$
Hanks et al. [1975]										
Ben-Menahem [1978]	S wave		050	80	65 x 34	(15[a])	NE	1.2[b]		8.4
										$M_w = 7.25$
Dunbar et al. [1980]	geodetic	SW shallow	050	60	35	0	5	0.24 ± 0.04	-0.33 ± 0.05	9.3
		NE shallow			35	0	5	0.28 ± 0.05	0.71 ± 0.07	$M_w = 7.27$
		SW deep			35	5	20	1.9 ± 0.08	2.5 ± 0.08	
		NE deep			35	5	20	0.58 ± 0.05	2.3 ± 0.10	
Stein and Thatcher [1981]	geodetic	SW	073	75	25	5.0	27	2.4	2.0	10.5
		Central	058	35	25	3.5	15	1.0	2.0	$M_w = 7.33$
		NE	043	20	25	2.0	10	0.4	1.0	
this study	geodetic	SW	051	75	29.7	6.0	27.0	1.61 ± 0.03	3.56 ± 0.28	9.2 ± 0.5
		NE	051	75	23.6	1.0	12.5	1.89 ± 0.04	0.22 ± 0.13	$M_w = 7.22$

[a]Mean focal depth.
[b]Average slip magnitude on plane.

determined greater reverse slip in the epicentral region (Table 5). Left-lateral strike-slip displacements for this study were up to 1.5 m greater than the other studies in the southwest and were significantly lower along the northeastern segment. The reason for the disagreement among the different models is likely from the geometry and placement of the fault models. Observed surface displacements from the Kern County earthquake are small and often contradictory [*Buwalda and St. Amand*, 1955] and so provide little information to discriminate among the models. Additionally, the spatial distributions of aftershock focal mechanisms also provide little insight with a mixed pattern of reverse, strike-slip, and oblique mechanisms throughout the region [*Dreger and Savage*, 1999]. Where the geodetic studies agree is that most of the slip occurred below 5 km for the southwestern half of the rupture and the upper and lower depth of the fault is shallower along the northeastern portion of the fault (Table 5).

The geodetic moment that I calculated is at the lower end of the range of both seismic and geodetic moments previously determined for the Kern County earthquake (Table 5). Observed surface breaks from the mainshock extend 12 km northeast of the preferred fault model. Since the geodetic network could not resolve slip beyond this fault patch, then the moment calculated in this study can be taken as a lower bound for the Kern County earthquake.

6.3. Implications

Surface displacements and geometry associated with the preferred model are consistent with the regional topography and the current tectonic structures along the White Wolf fault (Plate 1). The southwestern half of the fault has no discernible topographic relief, with the exception of Wheeler Ridge at the southwestern end of the fault. Conversely, the northeastern half of the fault has elevated topography in the hanging wall block with elevations as high as 2100 m, while the footwall block, for the most part, remains at an elevation of 200 m (Figure 1). The region with the greatest coseismic uplift and sharpest deformation gradient agrees well with the present-day topography (Plate 1). Even though the area of model maximum uplift does not directly correspond to the highest topography, it does include Comanche Point, a site of contemporary folding and thrust faulting (Figure 6 and Plate 1) [*Goodman and Malin*, 1992]. The preferred slip model has high left-lateral strike slip in the southwest (3.6 m) and minimal strike slip in the northeast (0.2 m). If this slip distribution pattern were typical of earthquakes along the White Wolf fault, then some structure would need to accommodate the differential strike slip between the two fault patches. The position and orientation of the Comanche thrust system is consistent with the regional shortening that would be expected with the strike slip differential that the preferred model produced. Aftershocks for the Kern County earthquake are compatible with northeast shortening across the Comanche thrust system [*Dreger and Savage*, 1999].

The steeply dipping fault patch along the northeastern portion of the fault is consistent with the present-day seismicity and provides structural continuity between the White Wolf fault and the Scodie lineament, a newly forming strike-slip fault that extends northeast from the White Wolf fault (Figure 1) [*Bawden et al.*, 1999]. Aftershocks immediately following the Kern County earthquake provide little structural control on the dip of

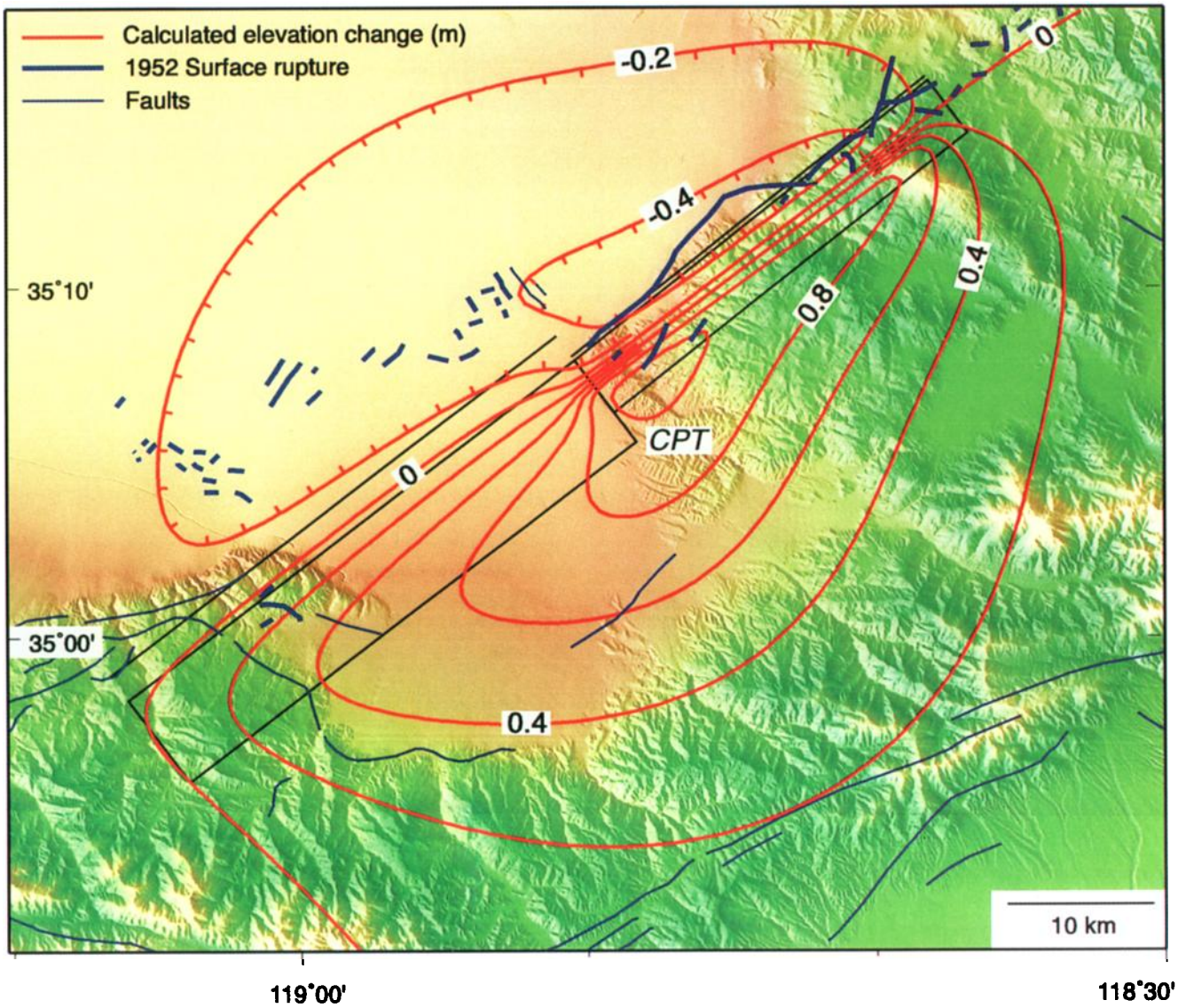

Plate 1. Comparison of modeled elevation changes and regional topography. Contours along the northeastern portion of the fault have been truncated to avoid covering all of the topography. CPT, Comanche Point thrust.

the northern fault because they lack a consistent pattern in the focal mechanism distribution [*Dreger and Savage*, 1999]. However, recent seismicity studies at the northern end of the White Wolf fault indicate predominantly strike-slip mechanisms on near-vertical planes, which is consistent with left-lateral shear along the White Wolf fault and the Scodie lineament [*Castillo and Zoback*, 1995; *Bawden et al.*, 1999]. The dip on the northern end of the Scodie lineament (75°-80°) is in good agreement with the preferred coseismic model (75°) and further suggesting that these structures are related.

7. Conclusions

Observations of coseismic elevation and angle changes associated with the 1952 Kern County earthquake favor a two-section right-stepping fault with deep (6-27 km) left-lateral oblique slip along the southwestern patch and shallow (1.0-12.5 km) reverse slip along the northeastern patch. The preferred source model has a strike of 051° and a dip of 75° to the southeast and a slip distribution pattern with nearly uniform reverse slip (1.6 and 1.9 m, southwest to northeast) along the length of the fault. Left-lateral strike slip was primarily limited to the southwestern half of the fault with 3.6 m. A resolution analysis of the data shows that the previous geodetic studies may have overestimated the resolution of the data by either subdividing the fault into multiple downdip patches or estimating slip on fault patches constrained by sparse data.

The coseismic slip model is supported by several geomorphic and structural features, as well as a kinematic fault model of southern California. The deep-seated strike slip along the epicentral patch correlates with both convergence and uplift in the Comanche Point region, an area of active folding and thrusting midway along the White Wolf fault. Furthermore, the region with the highest coseismic uplift and sharpest deformation gradient corresponds well to the present-day topography. The geometry of the northern end of the fault provides continuity with the Scodie seismic lineament to the northeast. Plate kinematic models from geologic and very long baseline interferometry

measurements for the greater San Andreas, Garlock, and White Wolf fault region show plate velocities orthogonal to the northeastern end of the fault, while the southwestern White Wolf and Pleito faults have a high component of left-lateral movement [*Saucier et al.*, 1993]. This is in good agreement with the coseismic model.

Acknowledgements. Discussion and reviews with Ross Stein and Wayne Thatcher provided valuable insights that greatly improved the manuscript. I thank Jim Savage, Will Prescott, and Chuck Wicks for their reviews, comments, and discussion. Jeff Freymueller, Mark Murray, and an anonymous reviewer provided thoughtful reviews that greatly improved the manuscript. I used inversion and dislocation modeling programs developed by Kathleen Hodgkinson and Shinji Toda. The earthquake locations were provided by the Southern California Earthquake Data Center and the Southern California Seismic Network, a joint project of the U.S. Geological Survey, Pasadena, and Seismological Laboratory, Pasadena. The GMT program [*Wessel and Smith*, 1991] was used to prepare a number of the figures.

References

Bawden, G. W., A. Donnellan, L. H. Kellogg, D. Dong, and J. B. Rundle, Geodetic measurements of horizontal strain near the White Wolf fault, Kern County, California, 1926-1993, *J. Geophys. Res., 102*(3), 4957-4967, 1997.

Bawden, G. W., A. J. Michael, and L. H. Kellogg, Birth of a fault: Connecting the Kern County and Walker Pass, California, earthquakes, *Geology, 27*(7), 601-604, 1999.

Ben-Menahem, A., Source mechanism of the 1906 San Francisco earthquake, *Phys. Earth Planet. Inter., 17*(2), 163-181, 1978.

Bomford, G., *Geodesy*, 452 pp., Clarendon, Oxford, England, 1980.

Buwalda, J. P., and P. St. Amand, Geological effects of the Arvin-Tehachapi earthquake, in *Earthquakes in Kern County California During 1952, Bull. 171*, edited by G. Oakeshott, pp. 41-56, Calif. Div. of Mines, San Francisco, 1955.

Castillo, D. A., and M. D. Zoback, Systematic stress variations in the southern San Joaquin Valley and along the White Wolf Fault: Implications for the rupture mechanics of the 1952 M_s 7.8 Kern County earthquake and contemporary seismicity, *J. Geophys. Res., 100*(4), 6249-6264, 1995.

Cisternas, A., Precision determination of focal depths and epicenters of local shocks in California, *Bull. Seismol. Soc. Am., 53*(5), 1075-1083, 1963.

Dreger, D., and B. Savage, Aftershocks of the 1952 Kern County, California, earthquake sequence, *Bull. Seismol. Soc. Am., 89*(4), 1094-1108, 1999.

Dunbar, W. S., D. M. Boore, and W. Thatcher, Pre-, co-, and postseismic strain changes associated with the 1952 M_L = 7.2 Kern County, California, earthquake, *Bull. Seismol. Soc. Am., 70*(5), 1893-1905, 1980.

Eberhart-Phillips, D., M. Lisowski, and M. D. Zoback, Crustal strain near the big bend of the San Andreas fault: Analysis of the Los Padres-Tehachapi trilateration networks, California, *J. Geophys. Res., 95*(2), 1139-1153, 1990.

Gergen, J. G., The new adjustment of the North American horizontal datum-the observables, *Am. Congr. Surv. Mapp. Bull., 51*, 9, 1975.

Goodman, E. D., and P. E. Malin, Evolution of the southern San Joaquin Basin and mid-Tertiary "transitional" tectonics, central California, *Tectonics, 11*(3), 478-498, 1992.

Gutenberg, B., The first motion on longitudinal and transverse waves of the main shock and the direction of slip, in *Earthquakes in Kern County California During 1952, Bull. 171*, edited by G. Oakeshott, pp. 165-170, Calif. Div. of Mines, San Francisco, 1955.

Hanks, T. C., J. A. Hileman, and W. Thatcher, Seismic moments of the larger earthquakes of the southern California region, *Geol. Soc. Am. Bull., 86*(8), 1131-1139, 1975.

Harris, R. A., and P. Segall, Detection of a locked zone at depth on the Parkfield, California, segment of the San Andreas fault, *J. Geophys. Res., 92*(8), 7945-7962, 1987.

Hodgkinson, K. M., R. S. Stein, and G. Marshall, Geometry of the 1954 Fairview Peak-Dixie Valley earthquake sequence from a joint inversion of leveling and triangulation data, *J. Geophys. Res., 101*(11), 25,437-25,458, 1996.

King, N. E., and J. C. Savage, Regional deformation near Palmdale, California, 1973-1983, *J. Geophys. Res., 89*(4), 2471-2477, 1984.

King, N. E., and W. Thatcher, The coseismic slip distribution of the 1940 and 1979 Imperial Valley, California, earthquakes and their implications, *J. Geophys. Res., 103*(8), 18,069-18,086, 1998.

Lofgren, B. E., Land subsidence due to ground-water withdrawal, Arvin-Maricopa area, California, *U.S. Geol. Surv. Prof. Pap., 437-D*, 55 pp., 1975.

Menke, W., *Geophysical Data Analysis: Discrete Inverse Theory*, 289 pp., Academic, San Diego, Calif.,1989.

Oakeshott, G. B., The Kern County earthquakes in California's geologic history, in *Earthquakes in Kern County California During 1952, Bull. 171*, edited by G. Oakeshott, pp. 15-22, Calif. Div.of Mines, San Francisco, 1955.

Richter, C. F., Foreshocks and Aftershocks, in *Earthquakes in Kern County California During 1952, Bull. 171*, edited by G. Oakeshott, pp. 177-198, Calif. Div. of Mines, San Francisco, 1955.

Ross, D. C., Basement-rock correlations across the White Wolf-Breckenridge-southern Kern Canyon fault zone, southern Sierra Nevada, California, *U.S. Geol. Surv. Bull., B 1651*, pp. 25, 1986.

Saucier, F., E. Humphreys, D. E. Smith, and D. L. Turcotte, Horizontal crustal deformation in Southern California from joint models of geologic and very long baseline interferometry measurements, in *Contributions of Space Geodesy to Geodynamics: Crustal Dynamics, Geodyn. Ser.*, vol. 23, edited by D. E. Smith, and D. L. Turcotte, pp. 139-176, AGU, Washington D. C., 1993.

Snay, R. A., M. W. Cline, C. R. Philipp, D. D. Jackson, Y. Feng, Z. K. Shen, and M. Lisowski, Crustal velocity field near the big bend of California's San Andreas fault, *J. Geophys. Res., 101*(2), 3173-3185, 1996.

Stein, R. S., and W. Thatcher, Seismic and aseismic deformation associated with the 1952 Kern County, California, earthquake and relationship to the Quaternary history of the White Wolf fault, *J. Geophys. Res., 86*(6), 4913-4928, 1981.

Thatcher, W., Horizontal crustal deformation from historic geodetic measurements in southern California, *J. Geophys. Res., 84*(B5), 2351-2370, 1979.

Thatcher, W. R., G. A. Marshall, and M. Lisowski, Resolution of fault slip along the 470-km-long rupture of the great 1906 San Francisco earthquake and its implications, *J. Geophys. Res., 102*(3), 5353-5367, 1997.

Wessel, P., and W. H. F. Smith, Free software helps map and display data, *Eos Trans., AGU, 72*(41), 441, 445-446, 1991.

Whitten, C. A., Measurements of Earth movements in California, in *Earthquakes in Kern County California During 1952, Bull. 171*, edited by G. Oakeshott, pp. 75-80, Calif. Div. of Mines, San Francisco, 1955.

G. W. Bawden, U.S. Geological Survey, 345 Middlefield Road, MS 977, Menlo Park, C 94025. (gbawden@usgs.gov)

(Received December 16, 1999; revised June 13, 2000;
accepted August 18, 2000.)